

# Multicycle terahertz pulse generation by optical rectification in LiNbO<sub>3</sub>, LiTaO<sub>3</sub>, and BBO crystals

Dogeun Jang and Ki-Yong Kim\*

Institute for Research in Electronics and Applied Physics, University of Maryland,  
College Park, MD 20742

\*kykim@umd.edu

May 26, 2020

## Abstract

We report multicycle, narrowband, terahertz radiation at 14.8 THz produced by phase-matched optical rectification of femtosecond laser pulses in bulk lithium niobate (LiNbO<sub>3</sub>) crystals. Our experiment and simulation show that the output terahertz energy greatly enhances when the input laser pulse is highly chirped, contrary to a common optical rectification process. We find this abnormal behavior is attributed to a linear electro-optic (or Pockels) effect, in which the laser pulse propagating in LiNbO<sub>3</sub> is modulated by the terahertz field it produces, and this in turn drives optical rectification more effectively to produce the terahertz field. This resonant cascading effect can greatly increase terahertz conversion efficiencies when the input laser pulse is properly pre-chirped with additional third order dispersion. We also observe similar multicycle terahertz emission from lithium tantalate (LiTaO<sub>3</sub>) at 14 THz and barium borate (BBO) at 7 THz, 10.6 THz, and 14.6 THz, all produced by narrowband phase-matched optical rectification.

## 1 Introduction

Intense, singlecycle, broadband terahertz (THz) sources are essential for many applications including THz-driven acceleration of electrons and protons [1, 2], molecular alignment [3], high harmonic generation [4], and material sciences [5]. In particular, femtosecond laser-based optical rectification (OR) in  $\chi^{(2)}$  nonlinear materials is considered to be one of the most efficient methods for energy-scalable THz generation [6]. OR can be highly effective when the group velocity of the laser pulse is matched to the phase velocity of the THz wave in the nonlinear medium—called phase matching. As an OR-based THz source, lithium niobate (LN) is widely used due to its excellent material properties such as high nonlinearities ( $d_{33} = 168$  pm/V at 1THz)[7], high transparency at  $0.4\sim 5$   $\mu\text{m}$  [8], and well-developed poling techniques [6]. For efficient phase matching in LN, tilted-pulse-front (TPF) schemes can be used to generate intense singlecycle THz pulses [7, 9, 10, 11].

Multicycle narrowband THz sources are also of great interest owing to many emerging applications including waveguide-based electron acceleration [12], coherent X-ray generation [13], resonant pumping of materials [3], and narrowband spectroscopy [6]. Multicycle narrowband THz radiation is often produced by OR in periodically-poled lithium niobate (PPLN) crystals [14, 15, 16, 17, 18]. Cryogenic cooled PPLN crystals are also used to suppress strong THz absorption in LN, lately providing a laser-to-THz conversion efficiency up to 0.1% [17]. Another approach is to drive OR with intensity-modulated laser pulses such that the produced THz waveform can follow the intensity envelope of the modulated laser pulse [19]. Other methods include transient polarization gratings [20], TPF planer waveguides [21], and cascaded second-order processes [22].

Recently, we have observed a new type of multicycle radiation at  $\sim 15$  THz emitted from a bulk LN crystal when irradiated by femtosecond laser pulses [23]. High-energy THz radiation up to 0.7 mJ has been also produced from a large diameter (75 mm) LN wafer with 80 TW laser pumping [24]. This type of radiation originates from a narrow phase matching condition naturally satisfied in between two phonon resonance frequencies in LN [23, 24]. Previously, similar narrowband radiation around 15 THz was produced by difference frequency generation (DFG) in LN, in which two separate laser pulses with different frequencies are mixed to generate THz radiation at the difference frequency [25]. By contrast, our THz generation method is based upon OR of a single laser pulse. This OR process is expected to produce higher THz energy with reducing laser driver's pulse duration. However, certain LN crystals exhibit enhanced THz radiation when driven by highly chirped laser pulses [24], contrary to our understanding of OR. Moreover, in the previous experiments, the radiation spectrum was poorly characterized with THz bandpass filter sets [24] or incompletely studied [23].

In this paper, we present a comprehensive study of multicycle narrowband THz generation around 15 THz from LN crystals. Experimentally, we measure THz field autocorrelation and spectral power under various laser conditions, especially when the laser driver is chirped with third order dispersion. To explain our experimental observation, we carry out numerical calculations on THz generation and propagation in LN. We also describe experimental measurements of chirp-dependent narrowband THz generation from lithium tantalate and barium borate crystals.

## 2 Experimental setup

The schematic of our experimental setup is shown in Fig. 1 (a). Femtosecond laser pulses from a Ti:sapphire amplifier operating at 1 kHz are loosely focused onto a LN crystal by a lens with a focal length of 1.5 m. The laser (pump) beam size ( $3.4\sim 6.8$  mm in  $1/e^2$  diameter) and fluence ( $3.2\sim 28.7$  mJ/cm<sup>2</sup>) are varied by translating the LN crystal along the beam propagation direction and/or controlling the laser energy. The pump pulse provides energies up to 2.6 mJ at a central wavelength of 800 nm with a 30 nm full-width half-maximum (FWHM) bandwidth as shown in Fig. 1(b). In our measurements, x-cut congruent LN crystals of  $10\text{ mm} \times 10\text{ mm} \times 0.5\text{ mm}$  or  $1\text{ mm}$  (thickness) are used for THz generation. The LN crystal is oriented such that its extraordinary axis is parallel

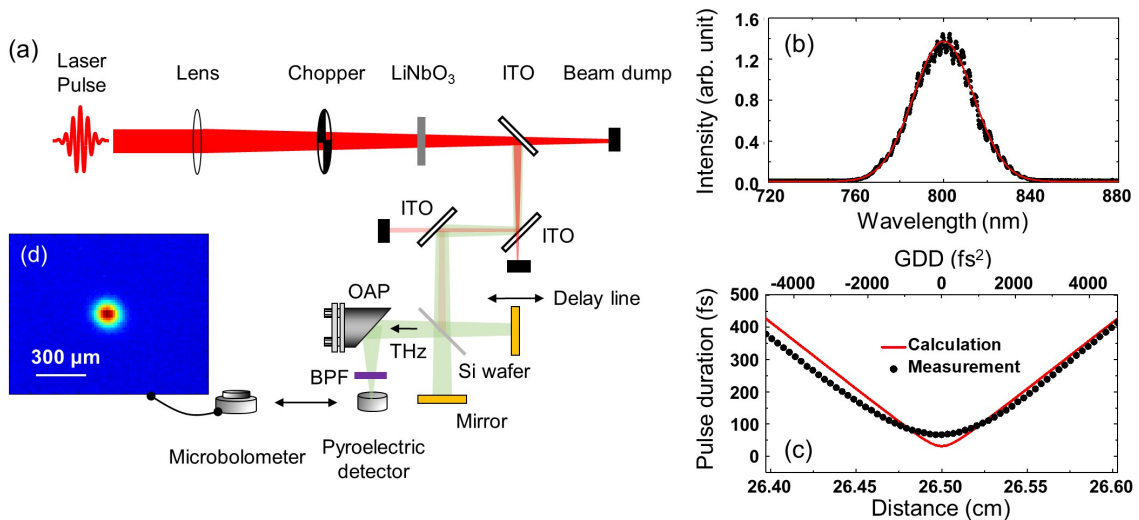


Figure 1: (a) Experimental setup for multicycle THz generation and detection. (b) Input laser spectrum measured (black line) before entering the experimental setup with a Gaussian fit (red line). (c) Measured (black dotted line) and estimated (red solid line) laser pulse duration as a function of input GDD, controlled by varying the distance between the grating pair in the laser compressor. (d) Focused THz beam profile captured by a microbolometer focal plane array.

to the laser polarization for maximal THz generation.

To decouple output THz pulses from the copropagating pump beam, three optical windows coated with 180-nm-thick indium thin oxide (ITO) are placed after the LN crystal. The ITO window allows high optical transmission ( $>85\%$  each) in the visible and near-infrared regions with strong reflection ( $\sim 80\%$  each) at  $<15$  THz [26]. Any pump leakage after the three ITO windows is completely blocked by a  $280\text{-}\mu\text{m}$ -thick high-resistivity ( $>10$  k $\Omega\cdot\text{cm}$ ) silicon (Si) window in the downstream beamline.

The resulting THz pulses are characterized by a lab-built Michelson-type Fourier-transform infrared (FTIR) interferometer combined with a pyroelectric detector (PD) (Spectrum Detector Inc., API-A-62-THz). The incoming THz beam is split and recombined with a variable time delay by a  $280\text{-}\mu\text{m}$  thick Si wafer in the interferometer and then focused by a  $90^\circ$  off-axis parabolic (OAP) mirror onto the PD detector. The THz signal from the PD detector is fed into a lock-in amplifier that is phase-locked to an optical chopper modulating the input laser beam at 10 Hz. A delay scan in the interferometer provides a THz field autocorrelation from which the spectral power can be obtained by the Fourier transform.

The pump pulse duration is varied by tuning the distance between the grating pair in the pulse compressor (see Appendix). This effectively changes the group delay dispersion (GDD) of the pump pulse. Figure 1(c) shows the pump pulse duration as a function of the grating distance. With a Gaussian spectral assumption, the Fourier transform-limited pulse duration is calculated to be  $\tau = 0.44\lambda_0^2/(c\Delta\lambda) \approx 31$  fs, where  $\lambda_0 = 800$  nm and  $\Delta\lambda = 30$  nm are the central wavelength and bandwidth in FWHM, respectively. With  $\text{GDD} = 0$  fs $^2$ , the pump pulse duration measured by a single-shot second-harmonic autocorrelator is about 67 fs in FWHM [dotted line in Fig. 1(c)]. This is longer than the transform-limited pulse duration of 31 fs. The difference is explained by uncompensated third order dispersion (TOD) and higher-order dispersion (HOD) of the pump pulse. Those result in an asymmetrical plot of the pulse duration as shown in Fig. 1(c). Figure 1(d) shows a typical THz intensity profile captured at the focus by a room-temperature microbolometer focal plane array (FLIR, Tau 2-336) [27, 28]. It shows that the focused THz radiation is confined within a spot size of  $160$   $\mu\text{m}$  in FWHM diameter.

### 3 Experimental results

#### 3.1 Broad and narrow band THz spectrum

Figure 2(a) shows THz autocorrelation signals obtained by the FTIR interferometer from the 1-mm-thick LN crystal with the pump fluence of  $12.8$  mJ/cm $^2$  and GDD of 0, 700, and 1,500 fs $^2$ . The corresponding THz spectral power is obtained by the Fourier transform and plotted in Fig. 2(b).

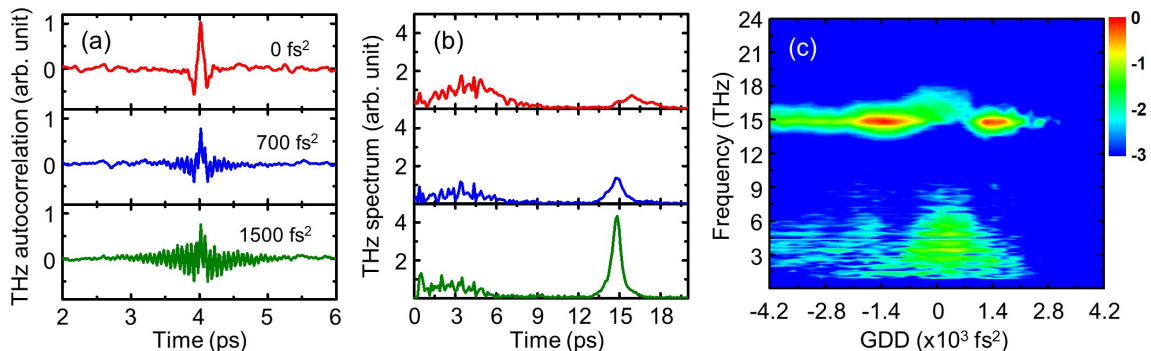


Figure 2: (a) Temporal THz autocorrelation signals measured at  $\text{GDD} = 0$  fs $^2$  (top), 700 fs $^2$  (middle), and 1,500 fs $^2$  (bottom). (b) Corresponding THz spectra. (c) Measured 2-D THz spectral power in a logarithmic scale (false color) as a function of the pump GDD (horizontal) and THz frequency (vertical).

For a series of GDD values, a two-dimensional (2-D) spectral power plot (color scale) is obtained and shown in Fig. 2(c). Figure 2 clearly shows two types of THz radiation emitted from LN—broadband singlecycle emission at 0~8 THz and narrowband multicycle emission around 15 THz. Interestingly, Fig. 2(c) shows that the narrowband emission is greatly enhanced with a properly stretched laser pulse duration (GDD =  $-800 \text{ fs}^2$ ,  $1,500 \text{ fs}^2$ ) whereas the broadband radiation is maximally produced with the shortest pulse duration (GDD  $\approx 0 \text{ fs}^2$ ).

The broadband THz emission has been previously observed and explained by non-phase-matched OR in LN through a second-order nonlinear  $\chi^{(2)}$  process [15, 16, 29]. This yields singlecycle THz pulses emitted from both the front and rear layers of LN with a thickness of one coherence length  $l_c = \lambda_{\text{THz}} / (2 |n_g - n_{\text{THz}}|)$  for each layer. Here  $n_g = 2.3$  is the optical group index of LN at 800 nm,  $n_{\text{THz}}$  is the refractive index of LN at THz frequencies, and  $\lambda_{\text{THz}}$  is the THz wavelength. At 1 THz,  $n_{\text{THz}} = 5.1$  [30, 8] and  $\lambda_{\text{THz}} = 300 \mu\text{m}$  gives  $l_c = 53.5 \mu\text{m}$ . This dual THz pulse generation explains the fast modulations observed in the broadband THz spectrum in Figs. 2(b) and 2(c). They arise due to interference between two temporally separated THz pulses generated from the front and rear surfaces of the LN crystal.

### 3.2 Characteristics of narrowband radiation at 15 THz

The narrowband multicycle radiation in Fig. 2 peaks at 14.8 THz with a 0.94 THz FWHM bandwidth at GDD =  $1,500 \text{ fs}^2$ . Its output energy dependence on the pump GDD is also measured and plotted in Fig. 3. Here the THz energy is measured by the pyroelectric detector (PD) along with a THz bandpass filter (BPF) providing a central frequency of 15 THz placed in front. This allows to measure only narrowband THz radiation around 14.8 THz.

As shown in Fig. 3, the output THz energy peaks at two GDD ranges of  $900 \sim 1,600 \text{ fs}^2$  (positive chirp) and  $-1,200 \sim -800 \text{ fs}^2$  (negative chirp). More interestingly, the positive GDD range yields more output THz energy with increasing pump energy and/or LN thickness. Furthermore, the output

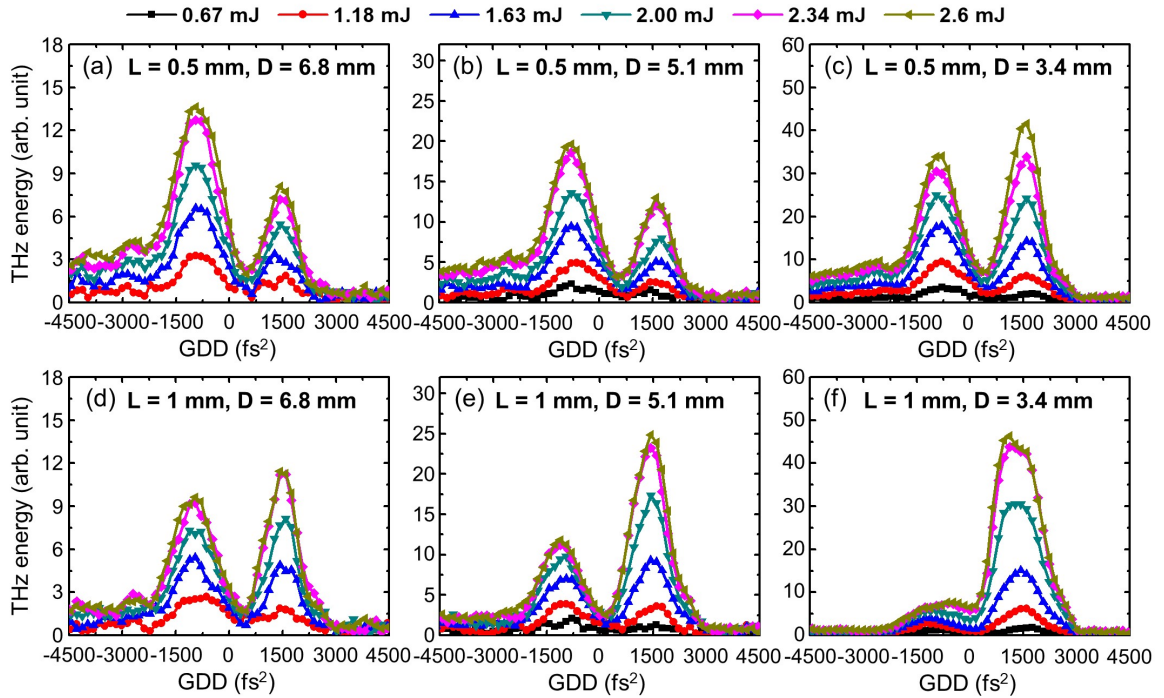


Figure 3: 15 THz emission energy measured as a function of the pump GDD from (a-c) 0.5-mm-thick and (d-f) 1-mm-thick LN crystals at various pump energies and beam sizes; L is the thickness of the LN crystal, and D is the FWHM pump beam size on the crystal.

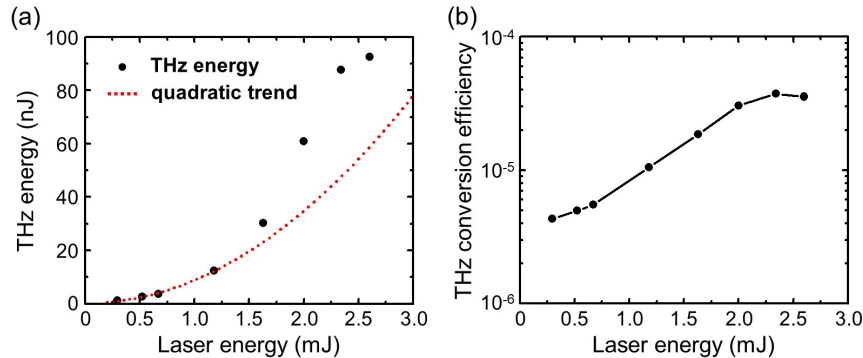


Figure 4: (a) Measured multicycle THz pulse energy as a function of the pump energy (black dots) obtained with  $L = 1$  mm and  $D = 3.4$  mm in Fig. 3(f), coplotted with a quadratic trend line (red dotted line) expected from OR. (b) Corresponding laser-to-THz conversion efficiency.

THz energy is abnormally suppressed at  $GDD \approx 0$  fs<sup>2</sup>, where the highest nonlinearity is expected due to the shortest pump pulse duration. Previously, similar results were observed and explained by THz screening and absorption by free charge carriers produced by multi-photon laser absorption in LN [11]. In our experiment, the nonlinear absorption coefficient by free carrier absorption (FCA),  $\alpha_{fc}$ , is estimated to  $31.63$  cm<sup>-1</sup> at  $14.8$  THz under laser conditions of  $470$  GW/cm<sup>2</sup> peak intensity and  $800$  nm wavelength [31, 32]. The value, however, is much smaller than the intrinsic absorption coefficient  $\alpha = 1,440$  cm<sup>-1</sup> at  $14.8$  THz in LN [23, 24]. Therefore, three-photon-absorption followed by FCA is not believed to cause the suppressed THz emission at  $GDD \approx 0$  fs<sup>2</sup>. Instead, the odd GDD-dependence can be explained by a THz-induced cascaded effect on the pump pulse that has nonzero TOD as will be described in Section 5.

Another interesting feature observed with the narrowband THz radiation is its energy scaling. Figure 4(a) shows the measured output THz energy emitted from the 1-mm-thick LN crystal as a function of the pump energy with the beam diameter of  $D = 3.4$  mm, corresponding to Fig. 3(f). In phase-matched OR, the output THz energy is expected to increase quadratically with the pump intensity, i.e.,  $e_{THz} \propto |I_{pump}|^2$ . This is indicated by the red-dotted line in Fig. 4(a). The observed THz energy, however, increases much faster than the theoretical prediction at the pump energy exceeding  $1.2$  mJ. This unexpected behavior can be also explained by a THz-induced cascaded effect as will be explained in Section 5.

The resulting laser-to-THz conversion efficiency is shown in Fig. 4(b). The maximum THz output energy of  $\sim 92.6$  nJ and efficiency of  $3.7 \times 10^{-5}$  are achieved. This provides a maximum field strength of  $0.4$  MV/cm at the focus, estimated from the measured energy, pulse duration ( $\sim 470$  fs), and beam spot size ( $\sim 160$   $\mu$ m).

### 3.3 Narrowband THz radiation from LT and $\beta$ -BBO crystals

Multicycle narrowband THz emission is also observed from lithium tantalate (LT) and beta-barium borate ( $\beta$ -BBO). These two nonlinear materials including LN are commonly used inorganic  $\chi^{(2)}$  nonlinear crystals and have a trigonal structure with point group 3m. LT and  $\beta$ -BBO are also tested for GDD-dependent THz generation, and the result is shown in Fig. 5. Figures 5(a) shows THz autocorrelation signals obtained from a 0.5-mm-thick LT crystal at two different pump GDD values of  $0$  and  $-1,100$  fs<sup>2</sup>. The corresponding spectra are shown in Fig. 5(b). From a GDD scan from  $-4,200$  fs<sup>2</sup> and  $4,200$  fs<sup>2</sup>, a 2-D plot of THz spectrum (color scale) is obtained and displayed in Fig. 5(c). Figures 5(d-f) shows experimental data obtained with a 0.1-mm-thick  $\beta$ -BBO crystal. For both measurements, the pump energy fluence is fixed at  $28.7$  mJ/cm<sup>2</sup>. Clearly, both crystals exhibit multicycle THz waveforms and consequent narrowband THz emission. In the case of LT, its narrowband emission is centered at  $14$  THz, consistent with the refractive index [33] and phase matching condition for LT. Similar to the LN crystals tested before, LT shows both singlecycle

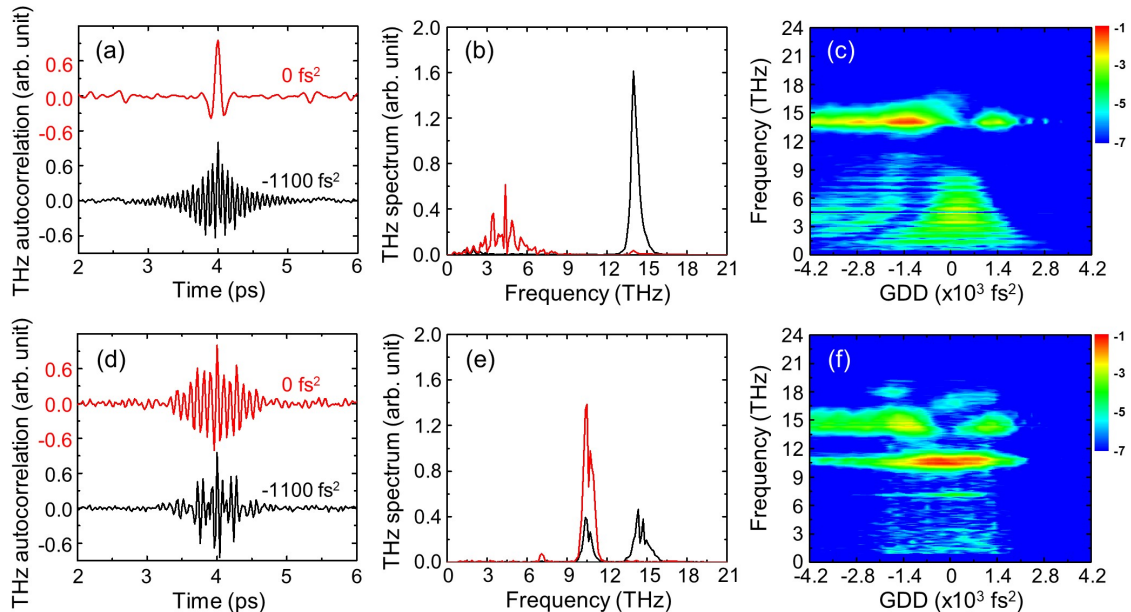


Figure 5: (a) Temporal THz autocorrelation signals measured from a 0.5-mm-thick LT crystal at  $\text{GDD} = 0 \text{ fs}^2$  (top red line) and  $-1,100 \text{ fs}^2$  (bottom black line). (b) Fourier-transformed THz spectra. (c) 2-D plot of THz spectrum (false color) measured as a function of the pump GDD. (d-f) Data measured with a 0.1-mm-thick  $\beta$ -BBO crystal.

(broadband) and multicycle (narrowband) radiation depending on the pump chirp condition.

The spectral power 2-D plot (color scale) of  $\beta$ -BBO shown in Fig. 5(f) exhibits narrowband emission at 7 THz, 10.6 THz, and 14.6 THz. Our result is consistent with a previous study reporting narrowband emission at 4.3 THz, 7 THz, and 10.6 THz [34]. Interestingly, 4.3-THz emission is not seen in our experiment possibly due to its weak spectral power. Instead, our experiment reveals new narrowband emission at 14.6 THz. We note that this observation was possible due to our FTIR-based detector's capability of measuring high-frequency THz emission beyond 10 THz. Contrary to commonly used electro-optic sampling (EOS) methods, in our scheme the detection bandwidth is not limited by the laser pulse duration or THz absorption/dispersion in the electro-optic (EO) material. Also, our detector is independent from the source and not affected by any pump chirp. This allows us to characterize the radiation spectrum without being distorted or restricted by the pump GDD.

## 4 Theoretical background

The narrowband THz radiation observed in Figs. 2 and 5 is fundamentally characterized by phase-matched ( $n_g = n_{\text{THz}}$ ) OR. Here  $n_g$  and  $n_{\text{THz}}$  are the group and refractive indices at the pump and THz frequencies, respectively. For example, Fig. 6(a) shows the refractive index  $n_{\text{THz}}$  of congruent LN as a function of frequency [8, 35, 36, 37] (see Appendix). The optical group index  $n_g = 2.3$  at 800 nm is also plotted in Fig. 3(a) with a gray dotted line. It shows that the phase-matching condition,  $n_g = n_{\text{THz}}$ , is satisfied at 14.8 THz in between two strong transverse-optical (TO) phonon resonance frequencies in LN (7.4 THz and 18.8 THz). These resonance frequencies are clearly shown by the absorption coefficient  $\alpha$  plotted in Fig. 3(a) with a red solid line. Note that there are two additional phase-matched frequencies occurring at 8.3 THz and 19.3 THz. However, little or no emission is expected at those frequencies because of their strong absorption in LN.

Figure 6(b) shows the effective nonlinear coefficient  $d_{\text{eff}}$  in the extraordinary direction of congruent LN [35, 36]. It shows  $d_{\text{eff}}$  reaches its local minimum value of 10 pm/V at 11 THz while peaking to

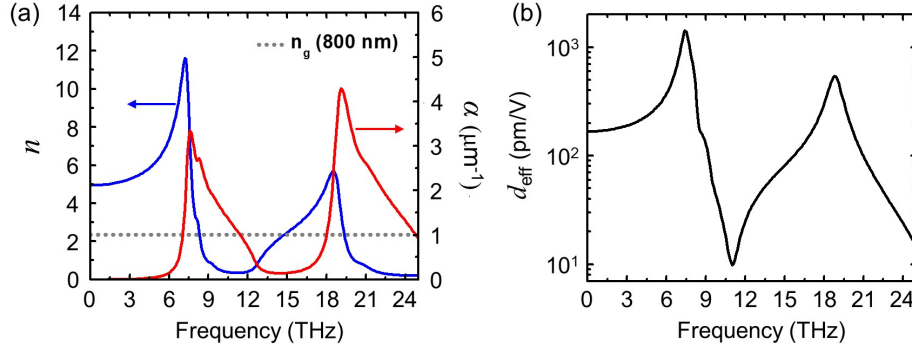


Figure 6: (a) Refractive index (blue solid line) and absorption coefficient (red solid line) of congruent LN in the extraordinary direction, co-plotted with the group index at 800 nm (gray dotted line). (b) Calculated effective nonlinear coefficient  $d_{\text{eff}}$  of LN in a logarithmic scale as a function of THz frequency.

1,424 pm/V and 543 pm/V at the two phonon resonance frequencies, 7.4 and 18.8 THz, respectively. At frequencies  $< 7.4$  THz,  $d_{\text{eff}}$  asymptotically approaches 168 pm/V, which is consistent with the reported value at 1 THz in Ref. [7]. At 14.8 THz,  $d_{\text{eff}} = 82$  pm/V, which is still sufficiently large to generate strong THz radiation [7, 32].

We emphasize this type of narrow phase matching can occur in many nonlinear crystals including LT and BBO. In general, the refractive index  $n_{\text{THz}}$  changes so large in between two phonon resonance, and often there exist one or multiple frequencies at which  $n_{\text{THz}}$  becomes equal to the optical group index of refraction  $n_g$ . Absorption is also expected to be relatively low in between phonon resonance frequencies. In addition, the phase-matched frequency can be tuned by varying the pump laser wavelength although it provides a narrow tuning range. For example, optical pumping at  $0.4 \sim 1.9$   $\mu\text{m}$  in LN can yield phase-matched emission at  $14.4 \sim 15.7$  THz.

At the phase-matched frequency of 14.8 THz in LN, the absorption coefficient reaches its minimum value of  $\alpha = 1,440$   $\text{cm}^{-1}$  as shown in Fig. 6(a). This value, however, is still large enough to attenuate the emission significantly. In phase-matched OR, the effective length for maximal THz generation is generally given by  $L_{\text{eff}} = (\alpha/2 - \alpha_L)^{-1} \ln[\alpha/(2\alpha_L)] \approx 160$   $\mu\text{m}$ , where  $\alpha_L = 0.0078$   $\text{cm}^{-1}$  is the laser absorption coefficient near 800 nm [24, 38]. This means that only a layer of 160  $\mu\text{m}$  thickness from the front surface of the LN crystal can maximally generate 14.8 THz radiation when the incident pump pulse is unchirped. In this case, a thin LN crystal is best suited for efficient THz generation as demonstrated in our previous experiment [24]. For thicker ( $\gg L_{\text{eff}}$ ) crystals as in the current experiment, negatively-chirped pump pulses are generally preferable as they can be compressed with propagation and effectively produce THz radiation from near the rear surface of the LN crystal.

Interestingly, our experiment shows that both positive and negative chirps yield enhanced THz emission as shown in Figs. 2 and 3. So it is the stretched pulse duration, not chirp, that matters in our narrowband THz generation. In general, too long pulses are not good as they do not provide enough bandwidths to generate 14.8 THz radiation by OR. For example, at  $\text{GDD} = 1,600$   $\text{fs}^2$  that yields enhanced 14.8 THz radiation, the corresponding pump pulse duration is estimated to  $\sim 130$  fs in FWHM from Fig. 1(c). This is about twice longer than the period of 14.8 THz radiation, 68 fs. This implies that the pump pulse must have certain intensity modulations (or pulse splitting) within the pulse envelope to provide a sufficient bandwidth to generate 14.8 THz. Such modulations can be initially made by applying a proper combination of GDD and TOD onto the pump pulse.

Pump intensity modulations can also arise and be amplified from a nonlinear process. For instance, a pump pulse propagating through LN can be distorted by the THz field it produces via a linear electro-optic (or Pockels) effect [39, 40]. This is a second-order  $\chi^{(2)}$  nonlinear process and can lead to spectral shifts, broadening, and modulations of the pump pulse [10, 39, 38]. Thus, in order to explain the peculiar GDD dependence of the narrowband radiation, one needs to include the Pockels

effect, as well as laser-THz dispersion and absorption in conducting numerical simulations.

## 5 Numerical simulations

### 5.1 Theoretical model

In order to simulate THz generation by OR, we first present the electric field of a laser (pump) pulse by using a Gaussian envelope shape given by

$$E(t) = E_0 \exp \left[ -\frac{\Delta\omega^2 t^2}{8 \ln 2} - j\omega_0 t \right], \quad (1)$$

where  $\omega_0$  is the center frequency,  $\Delta\omega = 4 \ln 2 / \Delta t$  is the FWHM spectral bandwidth, and  $\Delta t$  is the pulse duration in FWHM. The amplitude  $E_0$  is determined by the pump fluence  $F$  as

$$E_0 = \left( \frac{\ln 2}{\pi} \right)^{1/4} \sqrt{\frac{\Delta\omega F}{c\epsilon_0 n_0}}. \quad (2)$$

To account for chirped pump pulses, the spectral phase of the pump pulse is expanded in a Taylor series about  $\omega_0$  as

$$\phi(\omega) = \frac{\text{GDD}}{2} (\omega - \omega_0)^2 + \frac{\text{TOD}}{6} (\omega - \omega_0)^3, \quad (3)$$

where the fourth and higher-order terms are neglected for the sake of simplicity. The input pump pulse is obtained in the frequency domain as

$$E_p(\omega) = FT\{E(t)\} \exp[-j\phi(\omega)], \quad (4)$$

where  $FT$  denotes the Fourier transform.

Then we solve one-dimensional (1-D) coupled forward Maxwell equations (FME) [41, 29, 24] self-consistently for both THz and optical pump pulses in the frequency domain as

$$\begin{aligned} \frac{\partial E_T(\omega_T, \xi)}{\partial \xi} = & - \left( \frac{\alpha_T}{2} + jD(\omega_T) \right) E_T(\omega_T, \xi), \\ & - j \frac{\omega_T \chi^{(2)}}{2cn_0(\omega_T)} \int_0^\infty E_p(\omega + \omega_T, \xi) E_p^*(\omega, \xi) d\omega, \end{aligned} \quad (5)$$

$$\begin{aligned} \frac{\partial E_P(\omega, \xi)}{\partial \xi} = & - \left( \frac{\alpha_P}{2} + jD(\omega) \right) E_P(\omega, \xi), \\ & - j \frac{\omega \chi^{(2)}}{2cn_0(\omega)} \int_0^\infty E_P(\omega - \omega_T, \xi) E_T^*(\omega_T, \xi) d\omega_T, \\ & - j \frac{3\omega \chi^{(3)}}{8cn_0(\omega)} FT\{|E_P(t, \xi)|^2 E_P(t, \xi)\}, \end{aligned} \quad (6)$$

where  $E_T$  and  $E_P$  are the electric fields of THz and optical pump, respectively, which propagate in the coordinate  $\xi = z - ct/n_g$  moving at the group velocity of the pump. The first terms on the right hand side of both equations ( $\alpha$  terms) correspond to absorption of both fields. The second terms correspond to material dispersion  $D(\omega_T, \omega) = \omega(\omega_T, \omega) [n(\omega_T, \omega) - n_g] / c$ . The third term in Eq. (5) represents the second-order nonlinear polarization due to OR, a source term for THz radiation. The third term in Eq. (6) describes the Pockels effect on the pump pulse induced by the produced THz field. The last term in Eq. (6) corresponds to self-phase modulation (SPM) of the pump pulse via the Kerr effect, where the third-order nonlinear susceptibility  $\chi^{(3)}$  is derived from the nonlinear



refractive index  $n_2 = 3\chi^{(3)}/(4c\epsilon_0 n_0^2)$ . Here  $n_2 = 10^{-6}$  cm<sup>2</sup>/GW is used in our calculation [42]. In the simulation, we ignore THz-induced pump modulation via the  $\chi^{(3)}$  nonlinear process. This is because the  $\chi^{(3)}$ -based pump phase shift,  $\Delta\varphi^{(3)}$ , is much smaller than  $\Delta\varphi^{(2)}$  induced by the Pockels effect, i.e.,  $\Delta\varphi^{(3)}/\Delta\varphi^{(2)} = 3\chi^{(3)}E_{\text{THz}}/(2\chi^{(2)}) \ll 1$  [39].

The numerical integrals in Eqs. (5) and (6) are solved by a 4th-order Runge-Kutta method with spatial resolution of 500 nm in order to achieve required numerical convergences. Note that the model used here considers only 1-D space along the propagating direction  $z$ . This is justified for a large pump beam size, where any transverse beam effects such as self-focusing and diffraction can be ignored.

In the simulation, the input pump pulse is assumed to be Gaussian with a 30-nm FWHM spectral bandwidth at 800 nm to be consistent with our experimental condition. Experimentally, nonzero third order dispersion (TOD) arises from two sources; one is from the compressor’s tuning for GDD control (see Appendix). The other one comes from the amplifier itself but not properly compensated by the compressor. This residual TOD is implicitly shown in Fig. 1(c) by the asymmetric slope. Here the total TOD can be expressed as  $\text{TOD} = \text{TOD}_g + \text{TOD}_i$ , where the subscripts  $g$  and  $i$  denote “grating” and “initial (residual)”. In the simulation, we used  $\text{TOD}_g \approx -2(\text{fs}) \cdot \text{GDD}$  and  $\text{TOD}_i = 3,800 \text{ fs}^3$  for our compressor system (see Appendix).

## 5.2 Simulation results and discussions

### 5.2.1 GDD-dependent THz spectrum

We compare our simulation results with the experimental ones shown in Fig. 2. Figure 7(a) shows a simulated THz spectral power plot (color scale) obtained from a 1-mm-thick LN at laser fluence of 13.6 mJ/cm<sup>2</sup>. Clearly, it reproduces multicycle narrowband THz radiation around 15 THz. Also, it is most efficiently produced at  $\text{GDD} = 1,600 \text{ fs}^2$  and  $-800 \text{ fs}^2$ . At  $\text{GDD} \approx 0 \text{ fs}^2$ , it is greatly suppressed while the broadband radiation at 0~8 THz is maximally enhanced. This is in good agreement with our experimental results.

For comparison, we repeated the simulation with a chirped pump with  $\text{TOD}_i = 0 \text{ fs}^3$  to better understand the role of TOD in THz generation. The result is shown in Fig. 7(b). Interestingly, it shows the narrowband emission singly peaks at  $\text{GDD} = -800 \text{ fs}^2$ , and the maximal THz energy increases by 18.9% compared to Fig. 7(a). This does not agree with our experiment but is consistent with a general OR process, in which the radiated THz energy increases with decreasing pump pulse duration at fixed laser energy. Here a negatively chirped pump pulse is more favorable for THz generation because it can be compressed as it propagates through LN that possesses positive material dispersion. In addition, we repeated the simulation without including the Pockels effect but keeping the original TOD—the result is not shown in Fig. 7. In this case, maximal THz radiation occurs at  $\text{GDD} = -400 \text{ fs}^2$ , but the generated THz energy decreases to 62% compared to the first simulation

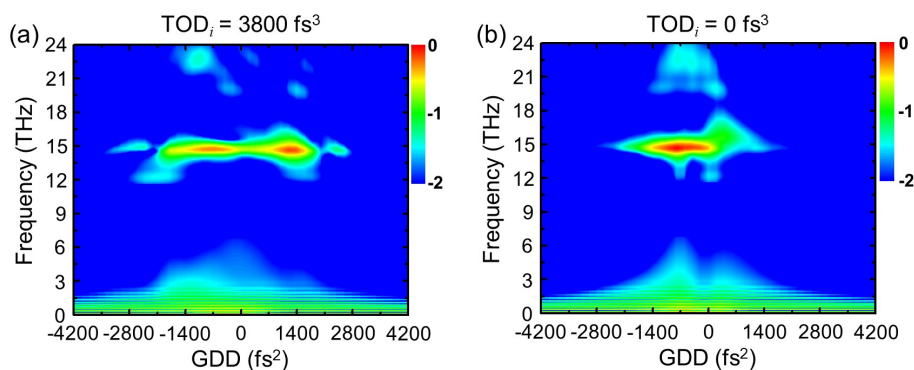


Figure 7: Simulated THz spectrum (false color) in a logarithmic scale as a function of the pump GDD (horizontal axis) obtained with (a)  $\text{TOD} = -2(\text{fs}) \cdot \text{GDD} + 3,800 \text{ fs}^3$  and (b)  $\text{TOD} = -2(\text{fs}) \cdot \text{GDD}$ .

result shown in Fig. 7(a). All these suggest that the strange GDD dependence of 15 THz observed in our experiment can be attributed to a combined action of both the Pockels and TOD effects.

### 5.2.2 Evolution of THz and laser fields with propagation

For a detailed understanding of multicycle THz generation, we simulated the evolution of THz electric fields and laser intensity envelopes as they propagate through LN. Here all simulation parameters are the same as in Fig. 7(a). First, Figure 8(a) shows the cumulative THz energy (color scale) plotted as a function of the initial GDD (vertical axis) and the propagation distance  $z$  (horizontal axis). Here the pump TOD varies as  $\text{TOD} = -2(\text{fs}) \cdot \text{GDD} + 3,800 \text{ fs}^3$ . Two line-outs at  $\text{GDD} = -800 \text{ fs}^2$  and  $1,600 \text{ fs}^2$  are plotted in Fig. 8(b). In the case of  $\text{GDD} = -800 \text{ fs}^2$ , the generated THz energy slowly increases and then decreases beyond  $z = 0.6 \text{ mm}$ . However, with  $\text{GDD} = 1,600 \text{ fs}^2$ , the energy noticeably increases after  $z = 0.3 \text{ mm}$ .

Figure 8(c) shows the THz electric fields (black lines) calculated at  $z = 0, 0.3, 0.6,$  and  $0.9 \text{ mm}$  with an initial GDD value of  $1,600 \text{ fs}^2$ . Also co-plotted (red lines) are the temporal derivatives of the pump intensity profiles,  $-dI(t, z)/dt$ . For reference, the input pump intensity profile  $I(t)$  is shown (blue line) at  $z = 0 \text{ mm}$ . Clearly, it exhibits damped intensity modulations on its tail due to nonzero GDD and TOD. Initially, this type of intensity modulations is not best suited for multicycle THz generation because its oscillation frequency is chirped and not fully matched to 14.8 THz. However, with a propagation, the pump envelope becomes synchronously modulated by the

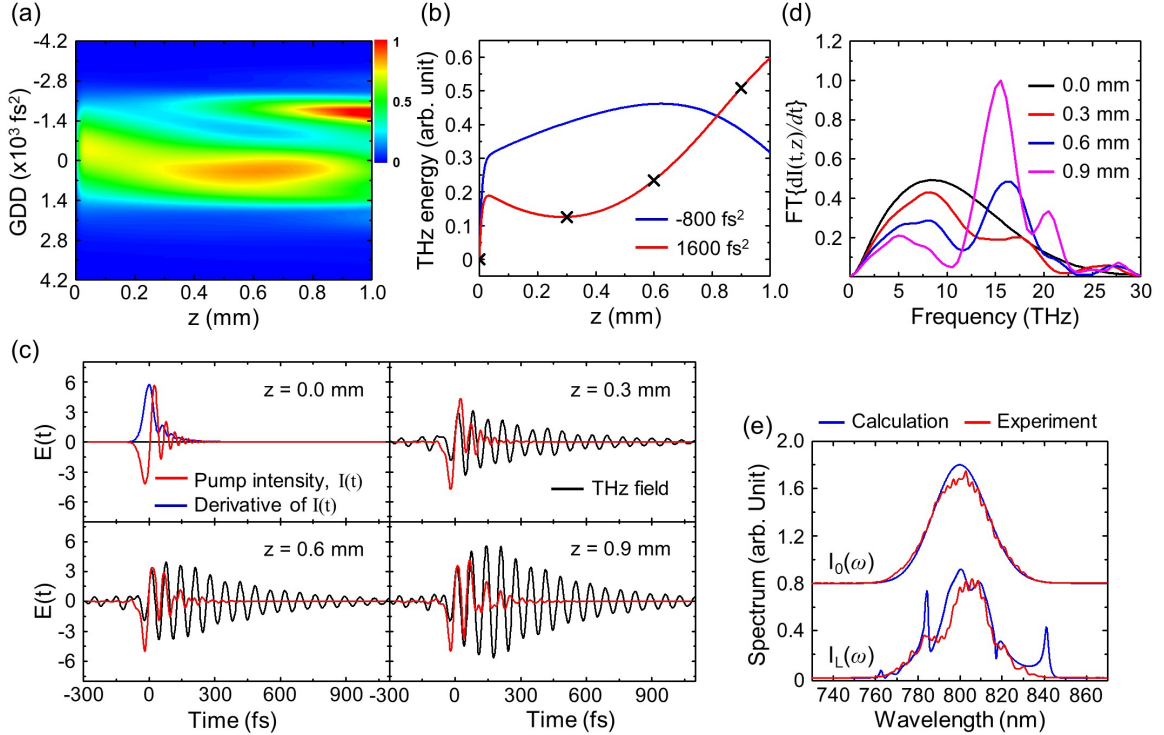


Figure 8: (a) Calculated multicycle THz energy (color scale) along the propagation direction  $z$  in LN for various initial GDD values. (b) Line-outs from (a) at  $\text{GDD} = -800 \text{ fs}^2$  (blue line) and  $1,600 \text{ fs}^2$  (red line). (c) THz waveforms (black lines) and pump intensity derivatives,  $-dI/dt$ , (red lines) computed at  $z = 0, 0.3, 0.6,$  and  $0.9 \text{ mm}$  (marked "X" in (b) with  $\text{GDD} = 1,600 \text{ fs}^2$ ). The input pump intensity profile  $I(t)$  is shown at  $z = 0 \text{ mm}$  (blue line). (d) Fourier-transformed spectra of the derivatives of pump intensity envelopes in (c). (e) Measured (red line) and simulated (blue line) pump spectra.  $I_0(\omega)$  and  $I_L(\omega)$  are the initial and final ( $z = 1 \text{ mm}$ ) spectra.

co-propagating 14.8 THz field via the Pockels effect. This results in a series of pump pulses (pulse splitting) separated by the THz period, which in turn drives OR resonantly to generate multicycle 14.8 THz radiation. This is evidently shown by the time derivative of the pump intensity envelope in Fig. 8(c) (red lines). Its Fourier spectral power at various  $z$  is plotted in Fig. 8(d). At  $z = 0.9$  mm, it peaks at  $\sim 15$  THz. It also produces two side bands. The left one is responsible for singlecycle broadband THz radiation at  $< 10$  THz, whereas the right (weak) one is believed to be the source of 20 $\sim$ 23 THz shown in Fig. 7(a) although it was not observed in our experiment.

Also, the input  $I_0(\omega)$  and transmitted  $I_t(\omega)$  pump spectra are computed and plotted in Fig. 8(e) along with experimentally measured ones. The transmitted one corresponds to a 1-mm-thick LN crystal pumped at 22 mJ/cm<sup>2</sup> with GDD = 1,500 fs<sup>2</sup>. As shown in Fig. 8(e), both simulated and measured pump spectra show spectral modulations and small frequency shifts. For negative GDD values, blue-shifted spectra are observed (not shown here).

Figure 9 shows the simulated output energy of multicycle THz radiation as a function of the pump GDD for 0.5-mm and 1-mm thick LN crystals. It shows that more output THz energy is produced at negative pump GDD values with a thinner (0.5 mm) LN. With increasing laser fluence and LN thickness (1.0 mm), however, the peak moves to the positive GDD side, consistent with our measurement in Fig. 3. Also, our simulation provides a laser-to-THz conversion efficiency of  $2.1 \times 10^{-5}$  from a 1-mm-thick LN pumped at 13.6 mJ/cm<sup>2</sup>. This is in reasonable agreement with our experimental value  $\sim 10^{-5}$  obtained under similar laser fluence conditions in Fig. 4(b).

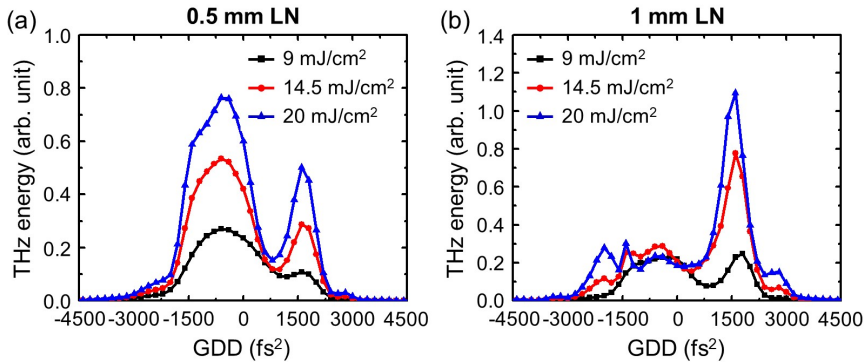


Figure 9: Simulated output energy of multicycle THz radiation as a function of the pump GDD for (a) 0.5-mm-thick and (b) 1-mm-thick LN crystals at three pump fluences.

## 6 Conclusion

In conclusion, we have demonstrated efficient multicycle narrowband THz generation at 14.8 THz from bulk LN crystals by using chirped optical pump pulses. The generation mechanism is explained by phase-matched OR naturally occurring in between two phonon resonance frequencies in LN. In our experiment, we have observed enhanced multicycle THz emission when the pump pulse is highly chirped. This anomalous behavior is also observed in our numerical simulations and explained by resonant intensity modulations of the pump pulse by self-produced THz fields through the Pockels effect. The modulated pump pulse can in turn produce multicycle THz radiation efficiently with propagation. This cascaded effect becomes highly efficient when the pump pulse is pre-modulated with proper second and third order dispersion. We also report the first demonstration of multicycle THz pulse generation at 14 THz from LT and 14.6 THz from  $\beta$ -BBO crystals. This new type of narrowband phase matching scheme is universal and can be applied to many nonlinear materials with potential to provide robust, efficient, and tabletop multicycle THz sources.

## 7 Appendix

### 7.1 Dispersion control in a dual grating compressor

In this experiment, the laser pulse duration is controlled by adjusting the separation between a pair of diffraction gratings in the pulse compressor. Right after the compressor, the second-order and third-order spectral phases of the laser pulse are given by [43]

$$\phi^{(2)} = -\frac{L\lambda^3}{\pi c^2 d^2} \left[ 1 - (\lambda/d - \sin \theta_{in})^2 \right]^{-\frac{3}{2}}, \quad (7)$$

$$\phi^{(3)} = -\phi^{(2)} \frac{3\lambda}{2\pi c} \left[ \frac{1 + \sin \theta_{in} (\lambda/d - \sin \theta_{in})}{1 - (\lambda/d - \sin \theta_{in})^2} \right], \quad (8)$$

where  $L$  is the perpendicular distance between the two parallel gratings,  $\theta_{in}$  is the incident laser angle, and  $d$  is the grating groove spacing. In our compressor system, we use 1,500 grooves/mm gratings at  $\theta_{in} = 58.4^\circ$  around a central wavelength of  $\lambda = 800$  nm. The second-order  $\phi^{(2)}$  and third-order  $\phi^{(3)}$  are generally referred to GDD and TOD, respectively. Figure 10 plots how GDD and TOD vary as a function of the grating separation  $L$  in our pulse compressor.

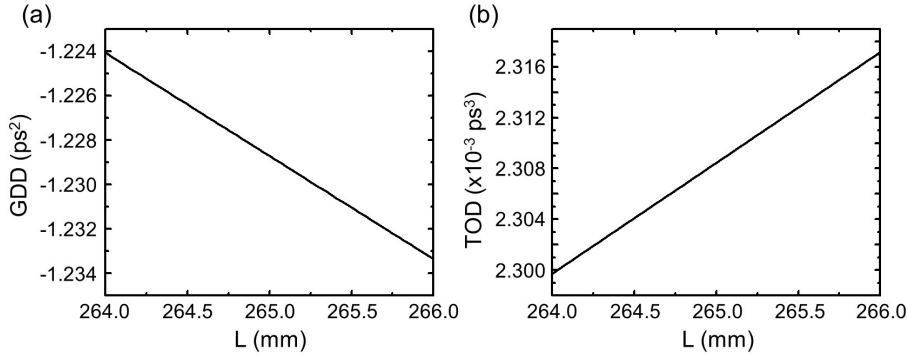


Figure 10: (a) Second-order spectral phase (GDD) and (b) third-order spectral phase (TOD) introduced by a dual grating compressor as a function of the separation between the grating pair.

For simplicity, Eq. (8) can be rewritten as  $\text{TOD} = A \cdot \text{GDD}$ , where  $A$  is a constant that depends on both the laser wavelength and incident angle, i.e.,  $A = A(\lambda, \theta_{in})$ . In our case, it is estimated to  $A \approx -2$  fs, and the shortest pulse duration is achieved with  $\text{GDD} = -1.229$  ps<sup>2</sup>. Thus, a “negative” or “positive” chirp is defined when GDD becomes less or greater than  $-1.229$  ps<sup>2</sup>, respectively.

### 7.2 Calculation of $\epsilon(\omega)$ and $d_{\text{eff}}(\omega)$ of lithium niobate

The complex dielectric function  $\epsilon(\omega)$  and nonlinear coefficient  $d_{\text{eff}}(\omega)$  of congruent LN are given by [37, 36]

$$\epsilon(\omega) = \epsilon_\infty + \sum_j \frac{S_j \omega_j^2}{\omega_j^2 - \omega^2 - i\omega\Gamma_j}, \quad (9)$$

$$d_{\text{eff}}(\omega) = d_e + \sum_j \frac{S_j \omega_j^2}{\omega_j^2 - \omega^2 - i\omega\Gamma_j} d_{Qj}, \quad (10)$$

where  $S_j$ ,  $\omega_j$ , and  $\Gamma_j$  are the oscillator strength, the resonance frequency, and the width of the  $j$ th transverse-phonon mode;  $\epsilon_\infty = 4.6$  is the frequency-independent bound electronic dielectric function;  $d_e$  and  $d_{Qj}$  are the electronic and ionic nonlinear coefficients, respectively. The real ( $n$ ) and imaginary ( $k$ ) parts of the square root of the complex dielectric function,  $\sqrt{\epsilon(\omega)} = n + ik$ , are

related to the refractive index  $n(\omega) = n$  and absorption coefficient  $\alpha(\omega) = 2k\omega/c$ . All parameter values necessary to calculate Eqs. (9) and (10) are listed in table 1.

Table 1: Properties of transverse modes in the extraordinary axis of LN. Additional modes at 3.9 THz and 20.76 THz are included to calculate the dielectric function.

$\omega_j/2\pi$ (THz)	$S_j$	$\Gamma_j/2\pi$ (THz)	$d_{Qj}$ (pm/V)	
3.9	5.7	0.69	-	[30]
7.44	16	0.63	7.66	[37, 36]
8.22	1	0.42	-14.68	[37, 36]
9.21	0.16	0.75	-17.87	[37, 36]
18.84	2.55	1.02	11.49	[37, 36]
20.76	0.13	1.47	-	[37]
	$\epsilon_\infty=4.6$ [37]		$d_e=33.7$ pm/V [36]	

### 7.3 TOD effects on multicycle THz pulse generation

To investigate the TOD effects, we repeated the simulation with various pump TOD values. In our experiment and simulation, the pump TOD varies with GDD as  $\text{TOD} = \text{TOD}_g + \text{TOD}_i = -2(\text{fs}) \cdot \text{GDD} + \text{TOD}_i$ . Figure 11 shows 2-D plots of narrowband THz energy (color scale) obtained with  $\text{TOD}_i$  of  $-4000$ ,  $-2000$ ,  $0$ ,  $2000$ , and  $4000$   $\text{fs}^3$ . The pump fluence is set to  $13.6$   $\text{mJ}/\text{cm}^2$ . For comparison, Fig. 8(a) is obtained with  $\text{TOD}_i = 3,800$   $\text{fs}^3$ .

As shown in Fig. 11, the output THz energy strongly depends on both GDD and TOD. With  $\text{TOD}_i = 0$   $\text{fs}^3$ , efficient THz generation occurs near  $\text{GDD} = 0$   $\text{fs}^2$  where the pump pulse duration remains relatively short. In this case, the energy rapidly increases but also quickly drops due to large THz absorption. Due to normal material dispersion in LN ( $368$   $\text{fs}^2/\text{mm}$  at  $800$  nm), more negative GDD is necessary to keep the pump pulse duration short with increasing propagation distance (or LN thickness). This is why the color plot in Fig. 11(c) has a single stripe with a negative slope. With large  $\text{TOD}_i$  values (either positive or negative), optimal THz generation occurs with relatively large GDD values (positive or negative) depending on the  $\text{TOD}_i$  sign and the propagation distance  $z$ . In this regime, the pump intensity envelop can be pre-modulated by a proper combination of GDD and TOD, and the modulation can be resonantly amplified through the cascaded Pockels effect.

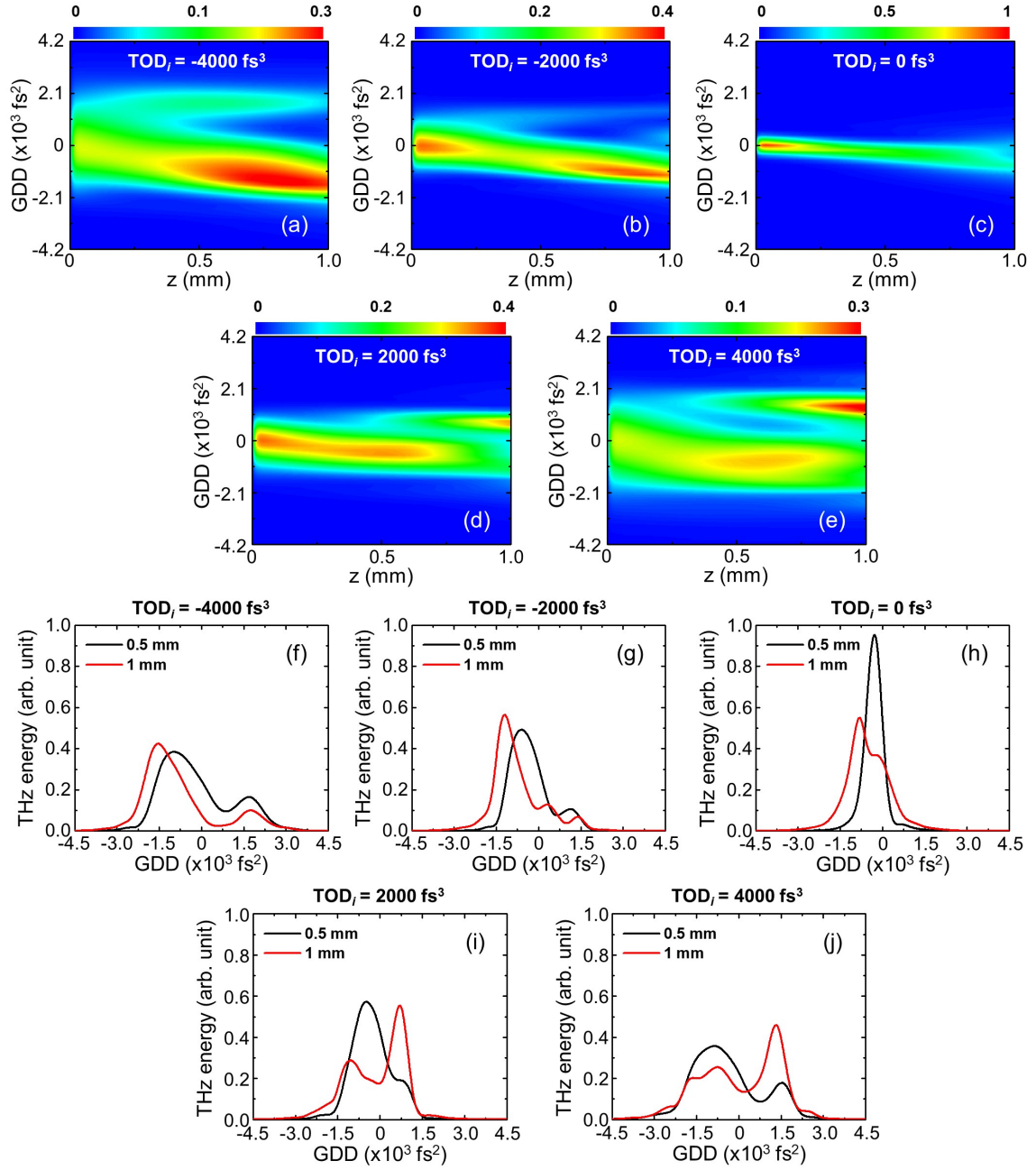


Figure 11: (a-e) 2-D plots of multicycle THz energy (color scale) as a function of the propagation direction  $z$  (horizontal) and initial pump GDD (vertical) with the initial (residual)  $\text{TOD}_i$  of -4000, -2000, 0, 2000, and 4000  $\text{fs}^3$ . (f-g) Line-outs at  $z = 0.5 \text{ mm}$  (black lines) and 1 mm (red lines).

## Funding

Air Force Office of Scientific Research (FA9550-25116-1-0163); Office of Naval Research (N00014-17-1-2705)

## References

- [1] Emilio A Nanni, Wenqian R Huang, Kyung-Han Hong, Koustuban Ravi, Arya Fallahi, Gustavo Moriena, RJ Dwayne Miller, and Franz X Kärtner. Terahertz-driven linear electron acceleration. *Nature Communications*, 6:8486, 2015.
- [2] L Pálfalvi, JA Fülöp, Gy Tóth, and J Hebling. Evanescent-wave proton postaccelerator driven by intense THz pulse. *Physical Review Special Topics-Accelerators and Beams*, 17(3):031301, 2014.
- [3] Tobias Kampfrath, Koichiro Tanaka, and Keith A Nelson. Resonant and nonresonant control over matter and light by intense terahertz transients. *Nature Photonics*, 7(9):680, 2013.
- [4] Olaf Schubert, Matthias Hohenleutner, Fabian Langer, Benedikt Urbanek, C Lange, U Huttner, D Golde, T Meier, M Kira, Stephan W Koch, et al. Sub-cycle control of terahertz high-harmonic generation by dynamical Bloch oscillations. *Nature Photonics*, 8(2):119–123, 2014.
- [5] Daniele Nicoletti and Andrea Cavalleri. Nonlinear light–matter interaction at terahertz frequencies. *Advances in Optics and Photonics*, 8(3):401–464, 2016.
- [6] Yun-Shik Lee. *Principles of Terahertz Science and Technology*, volume 170. Springer Science & Business Media, 2009.
- [7] János Hebling, Ka-Lo Yeh, Matthias C Hoffmann, Balázs Bartal, and Keith A Nelson. Generation of high-power terahertz pulses by tilted-pulse-front excitation and their application possibilities. *Journal of the Optical Society of America B*, 25(7):B6–B19, 2008.
- [8] Edward D Palik. Lithium niobate (LiNbO<sub>3</sub>). In *Handbook of Optical Constants of Solids*, pages 695–702. Elsevier, 1997.
- [9] József A Fülöp, Zoltán Ollmann, Cs Lombosi, Christoph Skrobol, Sandro Klingebiel, László Pálfalvi, Ferenc Krausz, Stefan Karsch, and János Hebling. Efficient generation of THz pulses with 0.4 mJ energy. *Optics Express*, 22(17):20155–20163, 2014.
- [10] Koustuban Ravi, W Ronny Huang, Sergio Carbajo, Xiaojun Wu, and Franz Kärtner. Limitations to THz generation by optical rectification using tilted pulse fronts. *Optics Express*, 22(17):20239–20251, 2014.
- [11] Xiao-Jun Wu, Jing-Long Ma, Bao-Long Zhang, Shu-Su Chai, Zhao-Ji Fang, Chen-Yi Xia, De-Yin Kong, Jin-Guang Wang, Hao Liu, Chang-Qing Zhu, et al. Highly efficient generation of 0.2 mJ terahertz pulses in lithium niobate at room temperature with sub-50 fs chirped Ti:sapphire laser pulses. *Optics Express*, 26(6):7107–7116, 2018.
- [12] Liang Jie Wong, Arya Fallahi, and Franz X Kärtner. Compact electron acceleration and bunch compression in THz waveguides. *Optics Express*, 21(8):9792–9806, 2013.
- [13] FX Kärtner, Frederike Ahr, A-L Calendron, H Çankaya, S Carbajo, G Chang, G Cirmi, K Dörner, U Dorda, A Fallahi, et al. AXSIS: Exploring the frontiers in attosecond X-ray science, imaging and spectroscopy. *Nuclear Instruments and Methods in Physics Research Section A: Accelerators, Spectrometers, Detectors and Associated Equipment*, 829:24–29, 2016.
- [14] Y-S Lee, T Meade, V Perlin, H Winful, TB Norris, and A Galvanauskas. Generation of narrow-band terahertz radiation via optical rectification of femtosecond pulses in periodically poled lithium niobate. *Applied Physics Letters*, 76(18):2505–2507, 2000.
- [15] JA L’huillier, G Torosyan, M Theuer, Yu Avetisyan, and R Beigang. Generation of THz radiation using bulk, periodically and aperiodically poled lithium niobate—Part 1: Theory. *Applied Physics B*, 86(2):185–196, 2007.

- [16] JA L’huillier, G Torosyan, M Theuer, C Rau, Yu Avetisyan, and R Beigang. Generation of THz radiation using bulk, periodically and aperiodically poled lithium niobate—Part 2: Experiments. *Applied Physics B*, 86(2):197–208, 2007.
- [17] Sergio Carbajo, Jan Schulte, Xiaojun Wu, Koustuban Ravi, Damian N Schimpf, and Franz X Kärtner. Efficient narrowband terahertz generation in cryogenically cooled periodically poled lithium niobate. *Optics Letters*, 40(24):5762–5765, 2015.
- [18] Spencer W Jolly, Nicholas H Matlis, Frederike Ahr, Vincent Leroux, Timo Eichner, Anne-Laure Calendron, Hideki Ishizuki, Takunori Taira, Franz X Kärtner, and Andreas R Maier. Spectral phase control of interfering chirped pulses for high-energy narrowband terahertz generation. *Nature Communications*, 10(1):2591, 2019.
- [19] Zhao Chen, Xibin Zhou, Christopher A Werley, and Keith A Nelson. Generation of high power tunable multicycle terahertz pulses. *Applied Physics Letters*, 99(7):071102, 2011.
- [20] AG Stepanov, J Hebling, and Juergen Kuhl. Generation, tuning, and shaping of narrow-band, picosecond THz pulses by two-beam excitation. *Optics Express*, 12(19):4650–4658, 2004.
- [21] Kung-Hsuan Lin, Christopher A Werley, and Keith A Nelson. Generation of multicycle terahertz phonon-polariton waves in a planar waveguide by tilted optical pulse fronts. *Applied Physics Letters*, 95(10):232, 2009.
- [22] Giovanni Cirimi, Michael Hemmer, Koustuban Ravi, Fabian Reichert, Luis E Zapata, Anne-Laure Calendron, Hüseyin Çankaya, Frederike Ahr, Oliver D Mücke, Nicholas H Matlis, et al. Cascaded second-order processes for the efficient generation of narrowband terahertz radiation. *Journal of Physics B: Atomic, Molecular and Optical Physics*, 50(4):044002, 2017.
- [23] Dogeun Jang, Yung Jun Yoo, and Ki-Yong Kim. Hidden phase-matched narrowband THz generation via optical rectification in lithium niobate. In *CLEO: Science and Innovations*, pages STh3F–4. Optical Society of America, 2019.
- [24] Dogeun Jang, Jae Hee Sung, Seong Ku Lee, Chul Kang, and Ki-Yong Kim. Generation of 0.7 mJ multicycle 15 THz radiation by phase-matched optical rectification in lithium niobate. *arXiv preprint arXiv:2003.11715*, 2020.
- [25] Xiaomu Lin, Lei Wang, and Yujie J Ding. Efficient generation of far-infrared radiation in the vicinity of polariton resonance of lithium niobate. *Optics Letters*, 37(17):3687–3689, 2012.
- [26] Ching-Wei Chen, Yen-Cheng Lin, Chia-Hua Chang, Peichen Yu, Jia-Min Shieh, and Ci-Ling Pan. Frequency-dependent complex conductivities and dielectric responses of indium tin oxide thin films from the visible to the far-infrared. *IEEE Journal of Quantum Electronics*, 46(12):1746–1754, 2010.
- [27] Yung-Jun Yoo, Donghoon Kuk, Zheqiang Zhong, and Ki-Yong Kim. Generation and characterization of strong terahertz fields from kHz laser filamentation. *IEEE Journal of Selected Topics in Quantum Electronics*, 23(4):1–7, 2016.
- [28] Dogeun Jang, Malik Kimbrue, Yung-Jun Yoo, and Ki-Yong Kim. Spectral characterization of a microbolometer focal plane array at terahertz frequencies. *IEEE Transactions on Terahertz Science and Technology*, 9(2):150–154, 2019.
- [29] Dogeun Jang, Chul Kang, Seong Ku Lee, Jae Hee Sung, Chul-Sik Kee, Seung Woo Kang, and Ki-Yong Kim. Scalable terahertz generation by large-area optical rectification at 80 TW laser power. *Optics Letters*, 44(22):5634–5637, 2019.
- [30] M Schall, H Helm, and SR Keiding. Far infrared properties of electro-optic crystals measured by THz time-domain spectroscopy. *Journal of Infrared, Millimeter, and Terahertz Waves*, 20(4):595–604, 1999.



- [31] Sen-Cheng Zhong, Zhao-Hui Zhai, Jiang Li, Li-Guo Zhu, Jun Li, Kun Meng, Qiao Liu, Liang-Hui Du, Jian-Heng Zhao, and Ze-Ren Li. Optimization of terahertz generation from LiNbO<sub>3</sub> under intense laser excitation with the effect of three-photon absorption. *Optics Express*, 23(24):31313–31323, 2015.
- [32] JA Fülöp, L Pálfalvi, G Almási, and J Hebling. Design of high-energy terahertz sources based on optical rectification. *Optics Express*, 18(12):12311–12327, 2010.
- [33] François Gervais and Vicente Fonseca. Lithium tantalate (LiTaO<sub>3</sub>). In *Handbook of Optical Constants of Solids*, pages 777–805. Elsevier, 1997.
- [34] David A Valverde-Chávez and David G Cooke. Multi-cycle terahertz emission from  $\beta$ -barium borate. *Journal of Infrared, Millimeter, and Terahertz Waves*, 38(1):96–103, 2017.
- [35] Yujie J Ding. Efficient generation of far-infrared radiation from a periodically poled LiNbO<sub>3</sub> waveguide based on surface-emitting geometry. *Journal of the Optical Society of America B*, 28(5):977–981, 2011.
- [36] Stanley Saul Sussman. Tunable light scattering from transverse optical modes in lithium niobate. Technical report, STANFORD UNIV CA MICROWAVE LAB, 1970.
- [37] AS Barker Jr and R Loudon. Dielectric properties and optical phonons in LiNbO<sub>3</sub>. *Physical Review*, 158(2):433, 1967.
- [38] Toshiaki Hattori and Kousuke Takeuchi. Simulation study on cascaded terahertz pulse generation in electro-optic crystals. *Optics Express*, 15(13):8076–8093, 2007.
- [39] Y Shen, T Watanabe, DA Arena, C-C Kao, JB Murphy, TY Tsang, XJ Wang, and GL Carr. Nonlinear cross-phase modulation with intense single-cycle terahertz pulses. *Physical Review Letters*, 99(4):043901, 2007.
- [40] Mukesh Jewariya, Masaya Nagai, and Koichiro Tanaka. Enhancement of terahertz wave generation by cascaded  $\chi^{(2)}$  processes in LiNbO<sub>3</sub>. *Journal of the Optical Society of America B*, 26(9):A101–A106, 2009.
- [41] AV Husakou and J Herrmann. Supercontinuum generation of higher-order solitons by fission in photonic crystal fibers. *Physical Review Letters*, 87(20):203901, 2001.
- [42] Richard DeSalvo, Ali A Said, David J Hagan, Eric W Van Stryland, and Mansoor Sheik-Bahae. Infrared to ultraviolet measurements of two-photon absorption and  $n_2$  in wide bandgap solids. *IEEE Journal of Quantum Electronics*, 32(8):1324–1333, 1996.
- [43] Frédéric Druon, Marc Hanna, Gaëlle Lucas-Leclin, Yoann Zaouter, Dimitris Papadopoulos, and Patrick Georges. Simple and general method to calculate the dispersion properties of complex and aberrated stretchers-compressors. *Journal of the Optical Society of America B*, 25(5):754–762, 2008.